Nuclear Science and Techniques (2026) 37:40
https://doi.org/10.1007/s41365-025-01878-y

Production of proton-rich isotopes of Pu, Cm, Bk, Ds, Cn, Fl by fusion evaporation reactions with ^{40}Ar projectile

Qing-Qing Yao[1] · Tian-Liang Zhao[1] · Xiao-Jun Bao[1]

Received: 10 November 2024 / Revised: 17 June 2025 / Accepted: 19 June 2025 / Published online: 9 January 2026

Abstract

The evaporation residual cross sections (ERCSs) of these reactions were calculated by using ^{144}Sm, ^{160,164}Dy, ^{165}Ho, ^{166}Er, ^{169}Tm, ^{171,174}Yb, ^{175}Lu, $^{176-180}$Hf, ^{181}Ta, ^{180,182}W and ^{187}Re targets with ^{40}Ar projectiles in the theoretical framework of the dinuclear system (DNS) model. The de-excitation process of the compound nucleus was theoretically calculated using two different statistical models, namely the statistical model 1 and statistical model 2 (GEMINI++ model). The calculated ERCSs were also compared with the experimental data. The ERCSs of synthesizing new proton-rich nuclides were investigated based on the fusion evaporation reaction. Predictions were made for the ERCSs of new isotopes of Pu, Cm and Bk in the heavy nuclei region, while the new isotopes of Ds, Cn and Fl are predicted in the superheavy nuclei region of $Z \geq 104$.

Keywords Dinuclear system model · Evaporation residue cross section · Proton-rich nuclides

1 Introduction

The synthesis of new elements and nuclides is a popular topic in the nuclear physics field [1–3]. This is not only of great significance for understanding the structure of matter, but also provides important information for understanding the evolution of the celestial environment, making it an essential means of exploring nature. Heavy-ion fusion evaporation (FE) reactions play a crucial role in the synthesis of new elements [3, 4] and nuclides [5, 6]. In such reactions [7, 8], heavy ions are accelerated by a heavy-ion accelerator and collide with target nuclei [9, 10], leading to nuclear fusion and subsequent evaporation processes that result in the synthesis of new nuclides [11, 12].

The FE reaction has made great progress in experiment. In 1975, ^{40}Ar beams with energies up to 225 MeV from the Dubna U-300 cyclotron bombarded ^{204}Pb and ^{206}Pb targets, and ^{242}Fm was synthesized [13]. The ^{206}Pb and ^{209}Bi targets were bombarded with ^{40}Ar beam from the GSI Universal Linear Accelerator (UNILAC) accelerator to form ^{243}Fm and ^{247}Md in the FE reactions in 1981 [14]. Similarly, the successful synthesis of new nuclides, ^{245}Md and ^{246}Md, was achieved via ^{40}Ar + ^{209}Bi combination at the GSI Laboratory in 1996 [15]. An enriched ^{204}Pb target was bombarded with ^{40}Ar beams from the GSI UNILAC accelerator, forming ^{241}Fm in the (3n) FE reaction in 2008 [16]. The new neutron-deficient isotope ^{217}U was produced in the bombardment of the ^{182}W target with ^{40}Ar ions and identified using a recoil-α-α correlation method in 2000 [17]. In addition, China has also made some achievements in the synthesis of new nuclides by using ^{40}Ar in recent years, such as the team of the Institute of Modern Physics of the Chinese Academy of Sciences (IMPCAS) successfully synthesizing the new uranium isotopes, ^{215,216}U, using the projectile-target combination ^{40}Ar + ^{180}W in 2015 [18, 19]. Since 2017, the IMPCAS has devoted itself to the synthesis and study of Np radioisotopes and has successively synthesized a series of new neutron-deficient isotopes ^{220,223,224}Np through the FE reactions ^{40}Ar + ^{185,187}Re [20–22].

This work was supported by the National Natural Science Foundation of China (Nos.12175064 and U2167203). Hunan Outstanding Youth Science Foundation (No. 2022JJ10031).

✉ Xiao-Jun Bao
baoxiaojun@hunnu.edu.cn

[1] Department of Physics, Collaborative Innovation Center for Quantum Effects, and Key Laboratory of Low Dimensional Quantum Structures and Quantum Control of Ministry of Education, Hunan Normal University, Changsha 410081, China

Recent results from Dubna for the ^{40}Ar + ^{238}U reaction [23] demonstrated that ^{40}Ar beam can also be used for the synthesis of superheavy nucleus.

In theoretical studies, many models have been developed to understand the formation mechanism of heavy and superheavy nuclei in FE reactions [24–28]. This study is based on the dinuclear system (DNS) model [29–32]. The synthesis of heavy and superheavy nuclei is a complex dynamic process involving competition between fusion and quasi-fission. The fusion and quasi-fission processes can be viewed as the evolution of the DNS model along the two main degrees of freedom: the relative motion of nuclei in the interaction potential for the formation of DNS and the decay of the DNS (quasi-fission process) along the elongation degree of freedom (internuclear motion); the transfer of nucleons between two nuclei in the mass asymmetric coordinate system $\eta = \frac{A_1 - A_2}{A_1 + A_2}$, which is the process of diffusion of the excited system and leads to the formation of compound nuclei (CN). It is assumed that the two contacting nuclei always maintain their ground-state characteristics in the DNS [33–35]. In fact, the nuclei in the DNS are gradually deformed by the strong nuclear and Coulomb interactions between them. This deformation alters the masses of the nuclei and the interactions between them, which affects the further evolution of the system [36]. Therefore, it is usually not negligible. The concept of DNS must be improved by decreasing the approximation used to simplify the calculation. In this study, we numerically investigate the time-dependent dynamical deformations of interacting nuclei, which are coupled with nucleon transfer the nucleon transfer in the heavy-ion fusion reaction to form superheavy nuclei (SHN). In Ref. [37], it was mentioned that in addition to the asymmetry degree variables of neutrons and protons, quadrupole deformations of interacting nuclei are also taken as a dynamic variables and construct a new four-variable master equations. This means that the deformation and the nucleon transfer are always regarded as diffusion processes controlled by the master equation in the potential energy surface of the system.

Theoretical calculations were performed using the combination of the DNS + statistical model 1, as well as the combination of the DNS + statistical model 2 (GEMINI++ model). The evaporation residual cross sections (ERCSs) for FE reactions were calculated by using ^{144}Sm, ^{160,164}Dy, ^{165}Ho, ^{166}Er, ^{169}Tm, ^{171,174}Yb, ^{175}Lu, $^{176-180}$Hf, ^{181}Ta, ^{180,182}W and ^{187}Re targets with ^{40}Ar projectile and the results were compared with available experimental data. The remainder of this paper is organized as follows. In Sect. 2, we give a brief description of the theoretical framework. The results and discussion are presented in Sect. 3. A summary is concluded in Sect. 4.

2 Theoretical framework

In theoretical studies, the FE reaction process can be divided into three successive phases. The first phase is the capture process, which can be evaluated using the capture cross section. The second phase is the evolution of the DNS from the contact configuration to the formation of a compound nucleus, which can be evaluated using the fusion probability. The final stage involves the excited compound nucleus undergoing evaporation of light particles to prevent fission, which can be evaluated using the survival probability. Finally, ERCSs of residual nuclei is obtained. In the DNS concept, the ERCS is calculated as the sum of all partial waves [24, 25, 38].

$$\sigma_{\mathrm{ER}} = \frac{\pi\hbar^2}{2\mu E_{\mathrm{c.m.}}} \times \sum_J (2J+1) T(E_{\mathrm{c.m.}}, J) P_{\mathrm{CN}}(E_{\mathrm{c.m.}}, J) W_{\mathrm{sur}}(E_{\mathrm{c.m.}}, J) \tag{1}$$

where $E_{\mathrm{c.m.}}$ and J are the incident energy and angular momentum in the center of mass coordinate system. The penetration probability $T(E_{\mathrm{c.m.}}, J)$ is the probability that the collision system overcomes the Coulomb barrier [39], and P_{CN} and W_{sur} denote the fusion probability and the survival probability, respectively.

The σ_{cap} is calculated using the empirical coupled-channel approach. Different potential distribution functions are constructed based on the different coupling modes between the projectile and target. They are divided into three cases: a fusion reaction involving two spherical nuclei, reactions with two statically deformed nuclei, and reactions with a combination of one spherical nucleus and one statically deformed nucleus, as described in detail in Ref. [40]. For a given center-of-mass energy $E_{\mathrm{c.m.}}$, the σ_{cap} $(E_{\mathrm{c.m.}},J)$ can be expressed as [41]:

$$\sigma_{\mathrm{cap}}(E_{\mathrm{c.m.}}, J) = \frac{\pi\hbar^2}{2\mu E_{\mathrm{c.m.}}} \sum_J (2J+1) T(E_{\mathrm{c.m.}}, J), \tag{2}$$

where μ denotes the reduced mass of the projectile and target nuclei. $T(E_{\mathrm{c.m.}}, J)$ is the penetration probability of the two colliding nuclei that overcome the Coulomb barrier in the entrance channel.

By numerically solving the four-variable master equations in the corresponding potential energy surface, the time evolution of the probability distribution function $P(Z_1, N_1, \beta_{12}, \beta_{22}, \theta_1, \theta_2, \varepsilon_1, \tau_{\mathrm{int}})$ under the directional angles (θ_1 and θ_2) can be obtained, which are mentioned in detail in Ref. [42–44]. Finally, the fusion probability P_{CN} is given by

$$P_{\mathrm{CN}}(E_{\mathrm{c.m.}},J)=\sum_{Z_1=1}^{Z_{\mathrm{BG}}}\sum_{N_1=1}^{N_{\mathrm{BG}}}\int_0^{0.6}\int_0^{0.6}\int_0^{\pi/2}\int_0^{\pi/2}P(Z_1,N_1,\beta_{12},\beta_{22},\theta_1,\theta_2,\tau_{\mathrm{int}})\rho_1(\beta_{12})\rho_2(\beta_{22})\sin\theta_1\sin\theta_2\mathrm{d}\beta_{12}\mathrm{d}\beta_{22}\mathrm{d}\theta_1\mathrm{d}\theta_2, \quad (3)$$

where N_{BG} and Z_{BG} are the Businaro-Gallone points. The quantities Z_1 and N_1 represent the number of protons and neutrons in the fragment 1, respectively, with excitation energy ε_1. The β_{i2} $(i=1,2)$ denotes the quadrupole deformations of the fragments. The integral of θ represents the weighted average of directional angles from 0° to 90°. $\rho_i(\beta_{i2})=1/h_i$ denotes the density of the discrete dots with the step length h_i $(i=1,2)$. The interaction time τ_{int} in the dissipative process of two colliding nuclei is determined using the deflection function method [45].

Survival probability is important for evaluating ERCS. In the de-excitation process of the CN, two different statistical models are employed for theoretical calculations: statistical model 1 and statistical model 2 (GEMINI++ model). In model 1, similar to neutron evaporation, the probability in the channel of evaporating the x-th neutron, the y-th proton and the z-th α particle is expressed as [46]

$$W_{\mathrm{sur}}(E^*_{\mathrm{CN}},x,y,z,J)=P(E^*_{\mathrm{CN}},x,y,z,J)\times\prod_{i=1}^{x}\frac{\Gamma_{\mathrm{n}}(E^*_i,J)}{\Gamma_{\mathrm{tot}}(E^*_i,J)}\prod_{j=1}^{y}\frac{\Gamma_{\mathrm{p}}(E^*_j,J)}{\Gamma_{\mathrm{tot}}(E^*_j,J)}\prod_{k=1}^{z}\frac{\Gamma_{\alpha}(E^*_k,J)}{\Gamma_{\mathrm{tot}}(E^*_k,J)}, \quad (4)$$

where $P(E^*_{\mathrm{CN}},x,y,z,J)$ denotes the realization probability when the excitation energy of the compound nucleus is E^*_{CN} and its angular momentum is J. The total width Γ_{tot} for CN decay is the sum of the partial widths of particle evaporation Γ_m ($m=\mathrm{n},\mathrm{p},\alpha,\gamma$ for neutron, proton, α particle, and γ emission, respectively), and fission Γ_{f}. The excitation energy E^*_s before evaporating the s-th particle is evaluated by

$$E^*_{s+1}=E^*_s-B^{\mathrm{n}}_i-B^{\mathrm{p}}_j-B^{\alpha}_k-2T_s \quad (5)$$

with the initial condition $E^*_1=E^*_{\mathrm{CN}}$ and $s=i+j+k$. The B^{n}_i, B^{p}_j, B^{α}_k are the separation energy of the i-th neutron, j-th proton, k-th α particle, respectively [47]. The relationship between the compound nuclear temperature T_s and the excitation energy can be expressed as

$$E^*_i=aT_i^2-T_i. \quad (6)$$

The probability $P(E^*_{\mathrm{CN}},x,y,z,J)$ of evaporating x-neutrons, y-protons, and z-α particles at the excitation energy E^*_{CN} and angular momentum J is calculated using the Jackson formula [48].

$$P(E^*_{\mathrm{CN}},s,J)=I(\Delta_s,2s-3)-I(\Delta_{s+1},2s-1), \quad (7)$$

where the quantities I and Δ are given by:

$$I(z,m)=\frac{1}{m!}\int_0^z u^m e^{-u}\mathrm{d}u, \quad (8)$$

$$\Delta_s=\frac{E^*_{\mathrm{CN}}-\sum_{i=1}^{s}B^{\nu}_i}{T_i}, \quad (9)$$

where B^{ν}_i is the separation energy of the evaporation of the i-th particle and $s(x,y,z)=x+y+z$.

The particle decay widths are evaluated with the Weisskopf's evaporation theory [49] as

$$\Gamma_{\nu}(E^*,J)=(2s_{\nu}+1)\frac{m_{\nu}}{\pi^2\hbar^2\rho(E^*,J)}\times\int_0^{E^*-B_{\nu}-\delta-\delta_{\mathrm{n}}-\frac{1}{a}}\varepsilon\rho(E^*-B_{\nu}-\delta_{\mathrm{n}}-E_{\mathrm{rot}}-\varepsilon,J)\times\sigma_{\mathrm{inv}}(\varepsilon)\mathrm{d}\varepsilon. \quad (10)$$

Here, s_{ν}, m_{ν} and B_{ν} are the spin, mass, and binding energy of the evaporating particle, respectively. $\rho(E^*-B_{\nu}-\delta_{\mathrm{n}}-E_{\mathrm{rot}}-\varepsilon,J)$ represents the level density of the residual nucleus after the parent nucleus with excitation energy E^* evaporates a particle with kinetic energy ε. The level density parameter a is obtained from Eq. (14). For neutron evaporation, where the compound nucleus is a nucleus with an odd mass number A (the neutron number is odd), δ_{n} is equal to $12/\sqrt{A}$, and in other cases, it is set to 0. Rotational energy can be expressed as $E_{\mathrm{rot}}=J(J+1)\hbar^2/2\xi$. The moment of inertia is given by $\xi=0.4MR^2$, where M and R represent the mass and radius of the nucleus, respectively. The inverse cross section is given by $\sigma_{\mathrm{inv}}=\pi R_{\nu}^2T(\nu)$ with the radius of $R_{\nu}=1.21[(A-A_{\nu})^{1/3}+A_{\nu}^{1/3}]$, and A_{ν} is the mass number of the evaporated particle. The penetration probability is set to unity for neutrons and $T(\nu)=(1+\exp(\pi(V_{\mathrm{C}}(\nu)-\varepsilon)/\hbar\omega))^{-1}$ for charged particles with $\hbar\omega=5$ and 8 MeV for protons and α particles, respectively.

The coulomb barrier calculation in the case of emission of charge particles, which can be as

$$V_{\mathrm{C}}=\frac{Z_{\mathrm{CN}-i}Z_ie^2}{r_i(A^{1/3}_{\mathrm{CN}-i}+A^{1/3}_i)}. \quad (11)$$

Here, for proton emitting $r_{\mathrm{p}}=1.7$ fm, and for α emitting $r_{\alpha}=1.75$ fm, this is described in detail in Ref. [50].

The fission width can be calculated with the Bohr-Wheeler formula as [51]

$$\Gamma_{\rm f}(E^*,J)=\frac{1}{2\pi\rho_{\rm f}(E^*,J)}\int_0^{E^*-B_{\rm f}-E_{\rm rot}-\delta-\delta_{\rm f}-\frac{1}{a_{\rm f}}}\frac{\rho_{\rm f}(E^*-B_{\rm f}-\delta_{\rm f}-E_{\rm rot}-\varepsilon,J){\rm d}\varepsilon}{1+\exp[-2\pi(E^*-B_{\rm f}-\delta_{\rm f}-E_{\rm rot}-\varepsilon)/\hbar\omega]}. \tag{12}$$

Here, we take $\hbar\omega = 2.2$ MeV for all the nuclei considered [52], $\delta_{\rm f}$ is the correction for the fission barrier in neutron evaporation, and $\delta_{\rm f} = 0$ in other cases. The $a_{\rm f} = 1.1a$. The pairing correction energy δ is set to be $-12/\sqrt{A}$ (odd-odd), 0(odd-A), $-12/\sqrt{A}$ (even-even), respectively. $B_{\rm f}$ is the fission barrier, consisting of the macroscopic and microscopic parts; more details are provided in Ref. [47].

The level density was calculated using the back-shifted Fermi-gas model [53]. The excitation energy is replaced with the equivalent excitation energy $U = E - \delta$. The energy level density is expressed as

$$\rho(U,J)=\frac{(2J+1)\exp\left[2\sqrt{aU}-\frac{(J+1/2)^2}{2\sigma^2}\right]}{24\sqrt{2}\sigma^3a^{1/4}U^{5/4}}, \tag{13}$$

with $\sigma^2=\frac{\Theta_{\rm rigid}}{\hbar^2}\sqrt{\frac{U}{a}}$, $\Theta_{\rm rigid}=\frac{2}{5}m_uAR^2$.

The selection of the level-density parameter in Eq. (13) is crucial, as it should be applied to both the low and high excitation energy regions. Only in this way can statistical model 1 be more rationally utilized to describe the de-excitation and fission processes of nuclei in the excited state. It is closely related to the excitation energy of the nucleus and shell correction.

$$a(U,Z,N)=\tilde{a}(A)\left[1+E_{\rm sh}\frac{f(U)}{U}\right] \tag{14}$$

$$\tilde{a}(A)=\alpha A+\beta A^{2/3} \tag{15}$$

$$f(U)=1-\exp(-\gamma_{\rm D}U) \tag{16}$$

The $\tilde{a}(A)$ is the asymptotic Fermi gas value of the level density parameter at a high excitation energy. It is worth noting that in Fermi gas models of the same type, different level density parameters mainly depend on the different shell corrections. Under the condition that the shell corrections are given by a certain mass formula, the values of the level density parameters are finally extracted by fitting all nuclei with experimental values of the level densities. In this study, the microscopic shell corrections from FRDM95 [54] were used to fit the experimental level density data, resulting in parameters $\alpha = 0.1337$, $\beta = -0.06571$, $\gamma_{\rm D}= 0.04884$ [55].

Another statistical model used in this study was GEMINI++, which is an improved version of the GEMINI statistical decay model developed by R. J. Charity [56] to describe the formation of complex fragments in heavy-ion fusion experiments. The de-excitation of the compound nucleus occurs through a series of binary decays until particle emission is energetically forbidden or impossible owing to competition with γ-ray emission. The evaporation process of light particles was described using the Hauser-Feshbach model in GEMINI++. In statistical model 1 and the GEMINI++ model, the same fission barrier was used. However, there are differences in the calculation methods for fission widths. In the GEMINI++ model, the Bohr-Wheeler formulism is used for symmetric fission [57]. For mass asymmetric fission outside the symmetric fission peak, the Moretto formalism is used. For statistical model 1, only Bohr-Wheeler's formula was used. In addition, there are differences in the treatment of level density and the parameters of level density between the two models. In GEMINI++, the level density is calculated using the Fermi gas model:

$$\rho(E^*,J)\sim\exp(2\sqrt{a(U)U}). \tag{17}$$

The level density parameter $a(U)$ is also related to the excitation energy. The excitation energy dependence is parameterized as follows:

$$\tilde{a}(U)=\frac{A}{k_\infty-(k_\infty-k_0)\exp(-\frac{\kappa}{k_\infty-k_0}\frac{U}{A})}, \tag{18}$$

where $k_0 = 7.3$ MeV, and the asymptotic value at high excitation energy is $\tilde{a}(U) = A/k_\infty$ ($k_\infty = 12$ MeV). The parameter κ defines how fast the long-range correlations wash out with the excitation energy. However, the fitting range of κ is small, and the maximum compound nucleus is only $A = 224$ [58]. The de-excitation process in this study was simulated using the GEMINI++ model, and the default parameters of this model were used for the calculations.

3 Numerical results and discussions

3.1 Production cross sections of heavy isotopes in ^{40}Ar induced reactions

A variety of new nuclides have been successfully synthesized in the proton-rich regions. Nevertheless, many unknown nuclides in this region are waiting to be explored. To further evaluate the potential of ^{40}Ar projectiles in the synthesis of new nuclides, we will continue to use ^{40}Ar as projectiles in subsequent theoretical calculations. The ERCSs for ^{40}Ar-induced reactions with target nuclei ^{144}Sm, ^{160,164}Dy, ^{165}Ho, ^{166}Er, ^{169}Tm, ^{171,174}Yb, ^{175}Lu, $^{176-180}$Hf, ^{181}Ta, ^{180,182}W and ^{187}Re are presented in Figs. 1–5, and compared them with available experimental data [18, 19, 21, 22, 59–61].

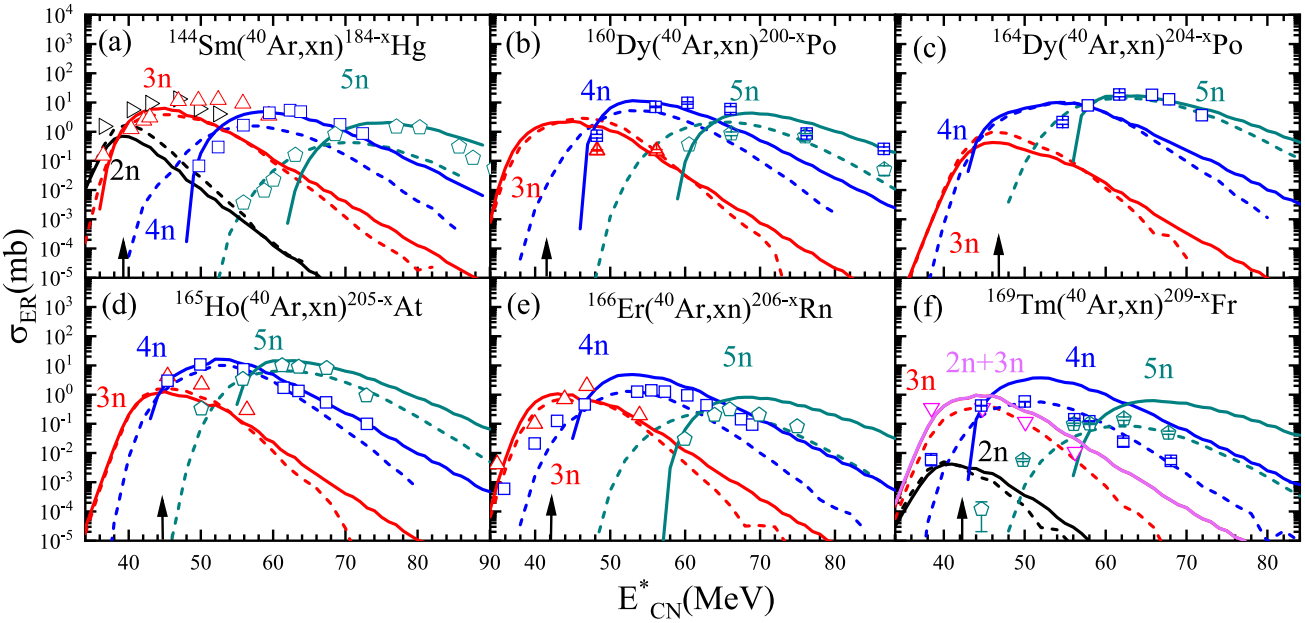

Fig. 1 (Color online) The ^{144}Sm, ^{160}Dy, ^{164}Dy, ^{165}Ho, ^{166}Er, ^{169}Tm targets were used with ^{40}Ar projectiles, the solid line indicates the ERCSs calculated with the DNS + statistical model 1, and the dashed part indicates the ERCSs derived using the DNS + GEMINI++ model. The different channels 2n, 3n, 4n, 5n, and 2n+3n are represented by black, red, blue, dark cyan, and pink, and the corresponding experimental data [59–61] are represented by hollow right-triangles (2n), up-triangles (3n), squares (4n), pentagons (5n), and down-triangles (2n+3n), respectively. The arrows show positions of the corresponding Coulomb barriers

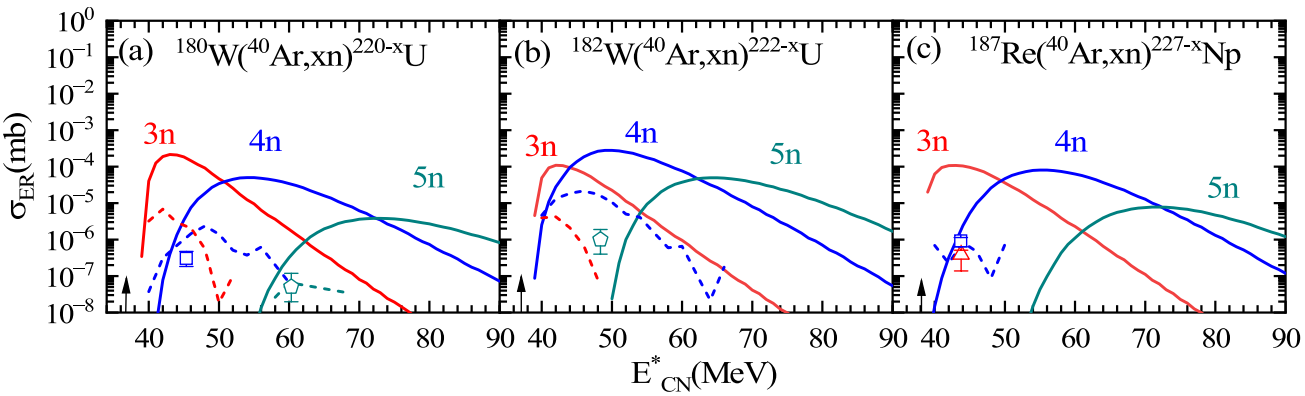

Fig. 2 (Color online) The ^{180}W, ^{182}W and ^{187}Re targets were used with ^{40}Ar projectiles. The different channels 2n, 3n, 4n, 5n are represented by black, red, blue and dark cyan, and the corresponding experimental values [18, 19, 21, 22] are represented by hollow up-triangles (3n), squares (4n), and pentagons (5n), respectively

The survival probabilities were calculated using two different statistical models for comparison. In Figs. 1–5, the solid lines indicate ERCSs calculated via the DNS + statistical model 1, the dashed lines indicate ERCSs derived using the DNS + GEMINI++ model, and hollow symbols indicate the relevant experimental data. The arrows show positions of the corresponding Coulomb barriers. The difference is that, as shown in Figs. 1 and 2, there is only the evaporation of pure neutrons and in Figs. 3–5 the evaporation of charged particles are included.

As can be seen in Fig. 1, the results of DNS+ statistical model 1 are slightly higher than those of DNS + GEMINI++ model. The results obtained by DNS + statistical model 1 and the DNS + GEMINI++ model were in good agreement with the experimental data for most evaporation channels of these reactions.

In the context of collision orientation, we have taken into account a weighted average over the range of 0° to 90°. As shown in Eq. 3, where the integral over the θ reflects the average effect of different collision

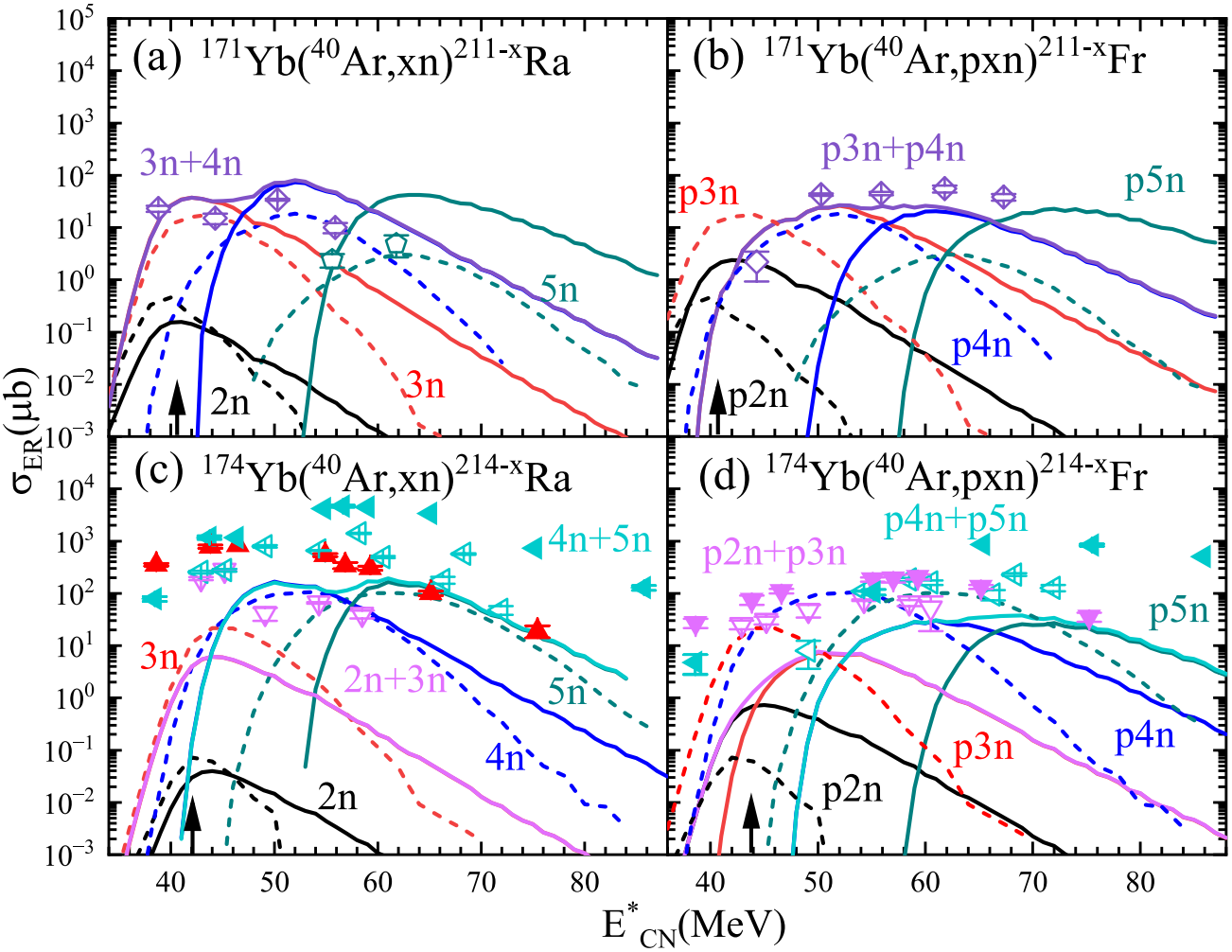

Fig. 3 (Color online) The ^{171,174}Yb isotopes were used with ^{40}Ar projectiles. The different channels 2n, 3n, 4n, 5n, 2n+3n, 3n+4n and 4n+5n are represented by black, red, blue, dark cyan, pink, purple and cyan, and the corresponding experimental data are represented by up-triangles (3n), down-triangles (2n+3n), rhombus (3n+4n), left-triangles (4n+5n), and pentagons (5n), respectively. The hollow symbols and solid symbols represent the experimental data from Ref. [59] and Ref. [61]

orientations. Consequently, the barrier height we calculated was an average value rather than a distribution. Furthermore, in the calculation of the fusion probability, the interaction time (τ_{int}) is required as an input. It can be seen from Eq. (11) in Ref. [62] that there is a value only when the incident energy ($E_{c.m.}$) is greater than the barrier. This also explains why the experimental data in the sub-barrier region cannot be reproduced.

Taking the reaction ^{40}Ar + ^{180}Hf as an example, Hinde et al. demonstrated, based on experimental data, that the fusion probability for ^{40}Ar + ^{180}Hf in above-barrier collisions is 0.15 [63]. The DNS model used in this study successfully reproduced the fusion probabilities at energies above the barrier but failed to describe the sub-barrier region. Both the experimental data and calculations using alternative models suggest that in the sub-barrier region, the fusion probabilities are not significantly lower than those at higher energies. This indicates that for the reactions involving ^{40}Ar + X considered in this study, the fusion probability is a slowly varying function of energy. Consequently, it is feasible to calculate the fusion probability within the energy range where the model is applicable. These calculations can then be extrapolated to lower energy levels starting a few MeV above the Coulomb barrier, using a physically functional form (here, we perform linear fitting processing on the fusion probabilities in the above barrier region).

It is evident from Fig. 1 that both statistical models provide a satisfactory description of the experimental data for the 3n evaporation channels in the reactions ^{40}Ar + ^{144}Sm, ^{40}Ar + ^{166}Er, as well as the 2n + 3n evaporation channel in the reaction ^{40}Ar + ^{169}Tm. Notably, the GEMINI++ model effectively reproduces the trend of the ERCS as a function of excitation energy in the 4n evaporation channel for the

^{40}Ar + ^{169}Tm reaction. For the 2n evaporation channel in the ^{40}Ar + ^{144}Sm reaction, the theoretical results closely aligned with the experimental data in both the sub-barrier and near-barrier regions. However, as the excitation energy increases, the survival probability decreases significantly, leading to ERCSs that are 2–3 orders of magnitude lower than the experimental data. By extrapolating the fusion probabilities using this method, the resulting ERCSs effectively reproduced the experimental data for the sub-barrier region.

Figure 2 shows the ERCSs for the ^{180}W(^{40}Ar, xn)$^{220-x}$U, ^{182}W(^{40}Ar, xn)$^{222-x}$U, ^{187}Re(^{40}Ar, xn)$^{227-x}$Np reactions. The results of DNS + statistical model 1 were higher than those of the GEMINI++ model. The computational ERCSs based on the GEMINI++ model were close to the relevant experimental data, and these results were in the same range as the experimental cross sections. However, a noticeable deficiency emerged in the GEMINI++ model calculations, manifesting as a lower number of generated events in these reactions.

To investigate the effect of different de-excitation processes of evaporating neutrons and charged particles on the ERCSs, we analyze different evaporation channels of the ^{40}Ar + ^{171,174}Yb, $^{176-180}$Hf, ^{175}Lu, ^{181}Ta reactions in Figs. 3, 4 and 5. In general, the production of certain isotopes is more likely to occur in the xn evaporation channel. However, the pxn and αxn evaporation channels allow us to access those isotopes that are unreachable in the xn channels owing to the lack of a proper projectile-target combination, as discussed in detail by Hong et al. [64]. This provides a new perspective for the synthesis of novel nuclides.

As shown in Figs. 3–5, for most channels of pure neutron evaporation, the DNS + statistical model 1 calculates ERCSs that are 1–2 orders of magnitude higher than those of DNS + GEMINI++ model. There is a difference of approximately 1–2 orders of magnitude between statistical model 1 and the experimental data, whereas the DNS + GEMINI++ model calculations are within 1 order of magnitude of the experimental data. Overall, the GEMINI++ model demonstrated superior performance in the neutron evaporation channels for these reactions. In the pxn evaporation channel, the differences between the calculations from the DNS + two statistical models were significantly reduced, and both were in good agreement with the experimental data. In the αxn evaporation channel, ERCSs calculated using DNS + GEMINI++ show significantly better agreement with the experimental data than those calculated using DNS + statistical model 1.

As mentioned in Sect. 2, the two statistical models differ in several aspects, which ultimately result in different survival probabilities for the different reaction systems. By comparing the ERCSs of the pure neutron evaporation channels and the charged particle evaporation channels (pxn and αxn) from Figs. 3–5, it is found that for the same projectile-target combination, the differences in ERCSs are mainly caused by different de-excitation modes. Specifically, these differences are mainly attributed to survival probability. It is worth noting that, based on Figs. 1–5, there are certain discrepancies between the theoretical calculations and experimental data for some evaporation channels.

The DNS model divides the fusion evaporation reaction into three consecutive processes, and the final ERCSs require comprehensive consideration of the impacts of various factors. It also involves certain assumptions and the selection of parameters. For example, our model requires a potential energy surface as an input when calculating fusion probabilities [65, 66]. However, calculating the multidimensional potential energy surfaces for the reaction system is a significant challenge in physics that has not yet been fully resolved. In addition, survival probabilities are calculated based on certain nuclear data, such as nuclear masses, neutron separation energies, and fission barriers (shell correction energies), which are usually extrapolated. For instance, in the calculation of the ERCSs for fusion reactions to synthesize SHN, the compound nucleus will evaporate 3–4 neutrons. When the fission barrier is imprecise, calculation errors in the neutron decay width and the ratio of fission width to (xn) de-excitation cascade at each step accumulate [67].

Additionally, it is important to note that our current model does not account for pre-equilibrium emission processes [68]. As is well known, this could be a significant concern at higher excitation energies. Hence, it may significantly alter the initial excitation energy distribution of the compound nucleus, making the theoretical prediction of the multi-neutron evaporation channels unreliable. Therefore, it is now calculated only for 5n evaporation channels.

Research has revealed that the production of new nuclides in the superheavy region primarily occurs through the neutron evaporation. The previous discussion shows that the two de-excitation models yield similar results in the pure neutron evaporation channels. The theoretical calculation of statistical model 1 was slightly higher than that of the GEMINI++ model. We found that the GEMINI++ model is able to better represent the survival process in the $Z = 82 - 92$ nuclear region and it also identified limitations of the GEMINI++ model in calculating survival probabilities in the actinide and superheavy nuclei regions. In addition, the number of simulations required is substantial, especially in the superheavy region where it reaches 1,000,000. Using the GEMINI++ model to simulate the de-excitation process is time-consuming. Therefore, we chose to use statistical model 1 for the generation of cross section prediction in the following parts B and C.

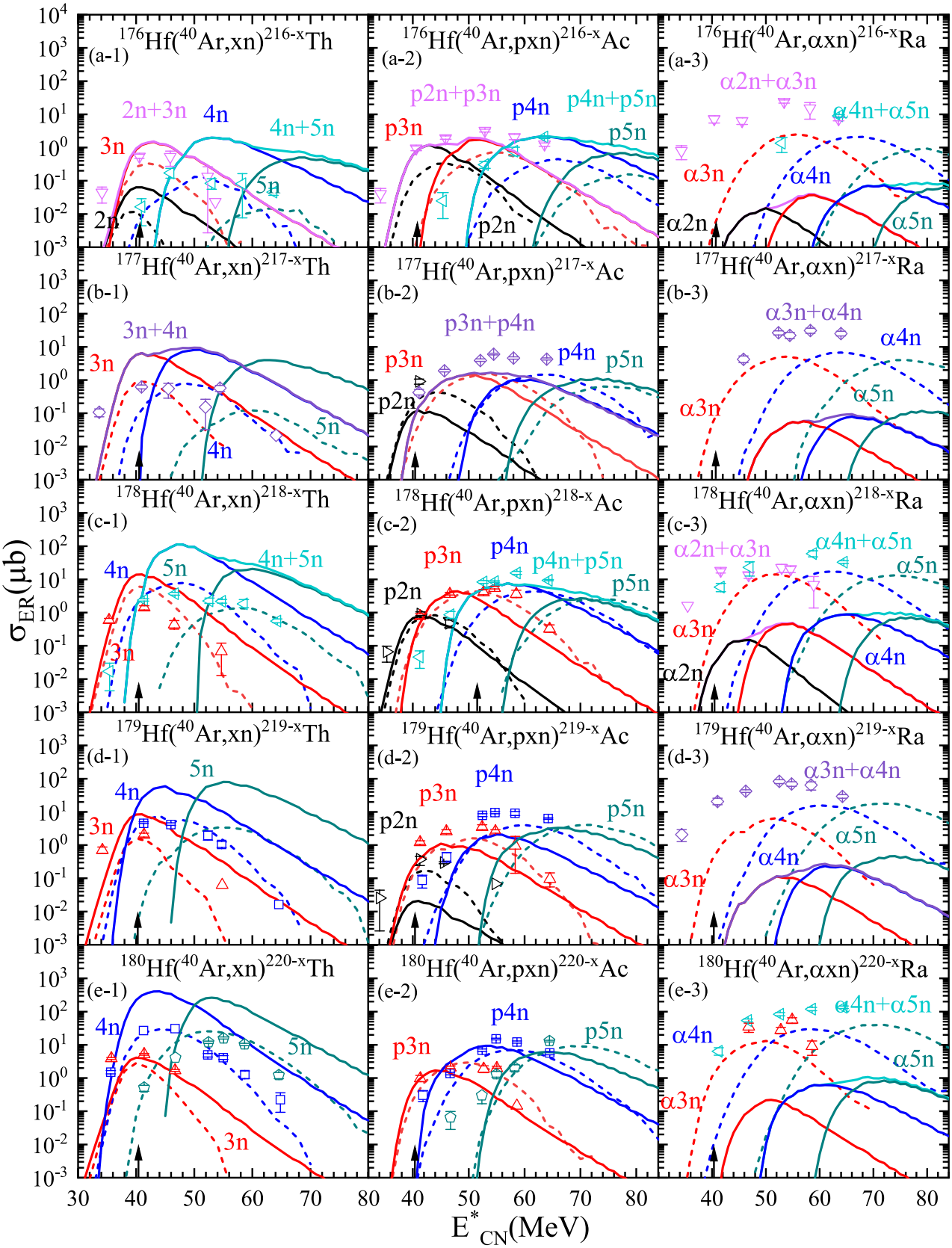
(a-1) 176Hf(40Ar,xn)216-xTh
2n+3n
4n
4n+5n
3n
5n
2n
(a-2) 176Hf(40Ar,pxn)216-xAc
p2n+p3n
p4n
p4n+p5n
p3n
p5n
p2n
(a-3) 176Hf(40Ar,αxn)216-xRa
α2n+α3n
α4n+α5n
α3n
α4n
α2n
α5n
(b-1) 177Hf(40Ar,xn)217-xTh
3n+4n
3n
5n
4n
(b-2) 177Hf(40Ar,pxn)217-xAc
p3n+p4n
p3n
p4n
p5n
p2n
(b-3) 177Hf(40Ar,αxn)217-xRa
α3n+α4n
α4n
α5n
α3n
(c-1) 178Hf(40Ar,xn)218-xTh
4n
5n
4n+5n
3n
(c-2) 178Hf(40Ar,pxn)218-xAc
p3n
p4n
p4n+p5n
p5n
p2n
(c-3) 178Hf(40Ar,αxn)218-xRa
α2n+α3n
α4n+α5n
α5n
α3n
α4n
α2n
(d-1) 179Hf(40Ar,xn)219-xTh
5n
4n
3n
(d-2) 179Hf(40Ar,pxn)219-xAc
p4n
p3n
p5n
p2n
(d-3) 179Hf(40Ar,αxn)219-xRa
α3n+α4n
α5n
α4n
α3n
(e-1) 180Hf(40Ar,xn)220-xTh
4n
5n
3n
(e-2) 180Hf(40Ar,pxn)220-xAc
p4n
p5n
p3n
(e-3) 180Hf(40Ar,αxn)220-xRa
α4n+α5n
α4n
α5n
α3n
σER(μb)
E*CN(MeV)

◂**Fig. 4** (Color online) The $^{176-180}$Hf isotopes were used with ^{40}Ar projectiles. The different channels 2n, 3n, 4n, 5n, 2n+3n, 3n+4n and 4n+5n are represented by black, red, blue, dark cyan, pink, purple and cyan, and the corresponding experimental values [59] are represented by hollow right-triangles (2n), up-triangles (3n), squares (4n), pentagons (5n), down-triangles (2n+3n), rhombus (3n+4n), and left-triangles (4n+5n), respectively

3.2 Production cross sections of Pu, Cm, Bk proton-rich isotopes in the heavy nuclear region

Based on the reliability of the theoretical calculations and to explore the potential of ^{40}Ar in synthesizing new isotopes, we will continue to use ^{40}Ar as the incident particle to further predict the ERCSs of new nuclides that could potentially be synthesized in the laboratory. Regarding the selection of ^{184}Os, ^{192}Pt and ^{197}Au as target materials, the primary reasons are as follows. First, these targets possess long half-lives, which ensures their stability over extended periods during experiments, enhancing efficiency and data reliability. Furthermore, when the ^{40}Ar beam bombards these target nuclei under the current experimental conditions, there is a possibility of producing new nuclides that are even more neutron-deficient. Figure 6 shows the relevant theoretical calculations obtained by the DNS + statistical model 1.

As shown in Fig. 6, for the ^{184}Os(^{40}Ar, xn) $^{224-x}$Pu reaction system, the maximum cross sections of 3n, 4n and 5n channels are 266.27, 176.53 and 31.63 pb, respectively, resulting in the production of $^{219-221}$Pu, and the maximum ERCS is located in the 3n channel, corresponding to the excitation energy of approximately 45 MeV. The maximum cross sections of 3n, 4n and 5n channels for ^{192}Pt(^{40}Ar, xn) $^{232-x}$Cm reaction are 177.34, 40.94 and 5.54 pb, respectively, resulting in the production of $^{227-229}$Cm. The maximum ERCS is located in the 3n channel, and the corresponding excitation energy is approximately 47 MeV. For ^{197}Au(^{40}Ar, xn)$^{237-x}$Bk reaction system, the maximum cross sections of 3n, 4n and 5n channels are 3193.41, 376.49 and 54.77 pb, respectively, resulting in the production of $^{232-234}$Bk. The maximum ERCS was located in the 3n channel, and the corresponding excitation energy was approximately 45 MeV.

3.3 Production cross sections of Ds, Cn, Fl proton-rich isotopes in the superheavy nuclear region

Similarly, we predicted the ERCSs of new nuclides in the superheavy nuclei region that may be synthesized in the laboratory. In this study, ^{40}Ar was utilized as the projectile with actinide targets, including ^{238}U, ^{244}Pu, and ^{248}Cm. In the field of superheavy nuclei research, ^{238}U, ^{244}Pu, and ^{248}Cm

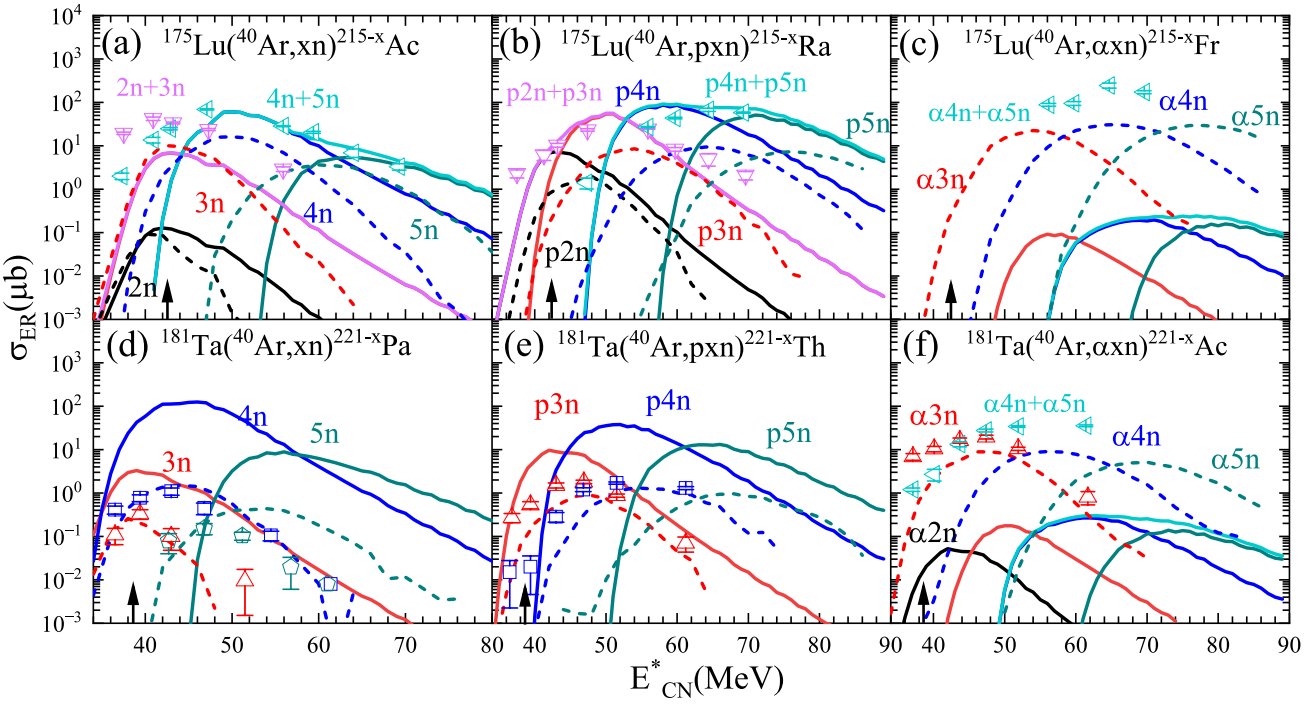

Fig. 5 (Color online) The ^{175}Lu and ^{181}Ta targets were used with ^{40}Ar projectiles. The different channels 2n, 3n, 4n, 5n, 2n+3n and 4n+5n are represented by black, red, blue, dark cyan, pink and cyan, and the corresponding experimental data [59] are represented by hollow up-triangles (3n), squares (4n), pentagons (5n), down-triangles (2n+3n), rhombus (3n+4n) and left-triangles (4n+5n), respectively

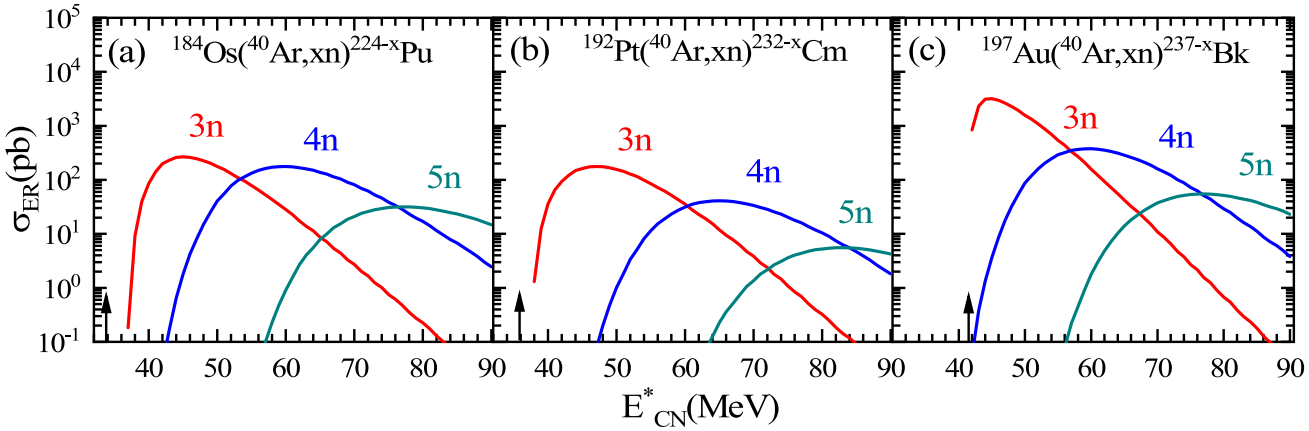

Fig. 6 (Color online) The ^{184}Os, ^{192}Pt, ^{197}Au targets were used with ^{40}Ar projectiles, the solid part indicates the ERCSs calculated with the DNS + statistical model 1. The different channels 3n, 4n, and 5n are represented by red, blue, and dark cyan, respectively

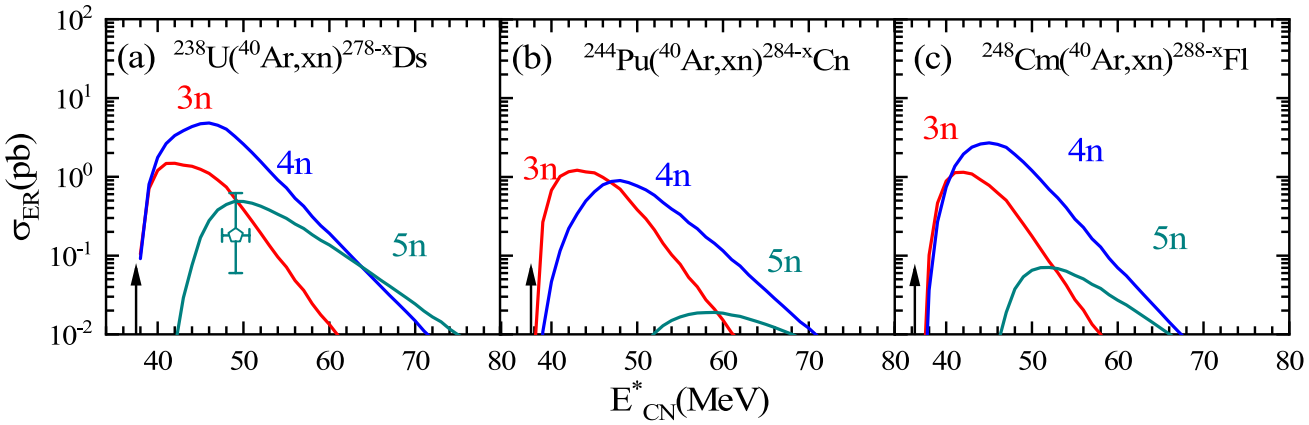

Fig. 7 (Color online) The ^{238}U, ^{244}Pu, ^{248}Cm targets were used with ^{40}Ar projectiles, the solid lines indicate the ERCSs calculated with the DNS + statistical model 1. The different channels 3n, 4n and 5n are represented by red, blue and dark cyan, respectively. The relevant experimental data[23] for the ^{238}U(^{40}Ar,5n)^{273}Ds are represented by hollow pentagons

are commonly used target nuclei, which have been validated by numerous experiments, particularly those involving ^{48}Ca beams. These studies have yielded invaluable data for understanding the properties of the superheavy elements.

Figure 7a shows the predicted excitation function of *x*n ERCSs for the reaction ^{238}U(^{40}Ar, *x*n) $^{278-x}$Ds. The maximal ERCSs of the 3n, 4n, and 5n channels were 1.479, 4.813, and 0.188 pb, respectively, resulting in the production of $^{273-275}$Ds. The largest ERCS was located in the 4n channel, with a corresponding excitation energy of 46 MeV. In particular, the new nuclide ^{273}Ds was produced through the combination of ^{40}Ar + ^{238}U with a production cross section of σ = 0.18 pb at an excitation energy of 49 MeV [23]. There is a 2.67 times difference compared to the theoretical result of 0.48 pb. In Fig. 7b, the maximum cross sections of the 3n, 4n and 5n channels of the ^{244}Pu(^{40}Ar, *x*n) $^{284-x}$Cn reaction are 1.215, 0.897 and 0.019 pb, respectively, resulting in the production of $^{279-281}$Cn. The largest ERCS is located in the 3n channel, and its corresponding excitation energy is approximately 43 MeV. Similarly, for the ^{248}Cm(^{40}Ar, *x*n)$^{288-x}$Fl reaction system in Fig. 7c, the maximum cross section of 3n, 4n and 5n channels are 1.142, 2.699 and 0.071pb, respectively, resulting in the production of $^{283-285}$Fl and the maximum residual evaporation cross section is located in the 4n channel, corresponding to the excitation energy of approximately 45 MeV. The new nuclides, such as $^{273-275}$Ds, ^{280,281}Cn, ^{284,285}Fl, are the most probable isotopes because of their larger cross sections.

4 Summary

Despite the fact that many areas of the nuclide chart have been filled in recent years, many unknown nuclides still exist in the nuclide chart. To search for proton-rich isotopes in heavy and superheavy regions, we systematically investigated the ^{40}Ar-induced fusion evaporation reaction in the theoretical framework of the DNS model. Two different statistical models were employed to calculate survival probabilities. The results indicated no significant differences between the two models in the computations of the neutron and proton evaporation channels. The GEMINI++ model showed superior performance in the calculations for α-particle evaporation channels. However, the GEMINI++ model has limitations in the SHN region. Based on statistical model 1, we used ^{40}Ar as projectiles to predict the ERCSs of new isotopes of actinide elements such as Pu, Cm and Bk. The cross sections of new isotopes of Ds, Cn, and Fl are predicted in the superheavy nuclei region of $Z \geq 104$. The production cross sections of $^{273-275}$Ds, $^{279-281}$Cn, $^{283-285}$Fl are 0.488, 4.813, 1.479 pb; 0.019, 0.89, 0.215 pb; 0.071, 2.699, 1.142 pb, respectively. We hope that these results will inspire further experimental studies on the synthesis of new isotopes.

Author contributions All authors contributed to the study conception and design. Material preparation, data collection and analysis were performed by Qing-Qing Yao, Tian-Liang Zhao, and Xiao-Jun Bao. The first draft of the manuscript was written by Qing-Qing Yao and all authors commented on previous versions of the manuscript. All authors read and approved the final manuscript.

Data availability The data that support the findings of this study are openly available in Science Data Bank at https://cstr.cn/31253.11.sciencedb.j00186.00850 and https://www.doi.org/10.57760/sciencedb.j00186.00850.

Declarations

Conflict of interest The authors declare that they have no Conflict of interest.

References

1. S.A. Giuliani, Z. Matheson, W. Nazarewicz et al., Colloquium: superheavy elements: oganesson and beyond. Rev. Mod. Phys. **91**, 011001 (2019). https://doi.org/10.1103/RevModPhys.91.011001
2. X.J. Bao, Y. Gao, J.Q. Li et al., Theoretical study of the synthesis of superheavy nuclei using radioactive beams. Phys. Rev. C **91**, 064612 (2015). https://doi.org/10.1103/PhysRevC.91.064612
3. S. Hofmann, G. Munzenberg, The discovery of the heaviest elements. Rev. Mod. Phys. **72**, 733 (2000). https://doi.org/10.1103/RevModPhys.72.733
4. S. Hofmann, Super-heavy nuclei. J. Phys. G: Nucl. Part. Phys. **42**, 114001 (2015). https://doi.org/10.1088/0954-3899/42/11/114001
5. S. Hofmann, F. Heßberger, D. Ackermann et al., New results on elements 111 and 112. Eur. Phys. J. A **14**, 147 (2002). https://doi.org/10.1140/epja/i2001-10119-x
6. K. Morita, K. Morimoto, D. Kaji et al., Experiment on synthesis of an isotope ^{277}112 by ^{208}Pb + ^{70}Zn reaction. J. Phys. Soc. Jpn. **76**, 043201 (2007). https://doi.org/10.1143/JPSJ.76.043201
7. Y.T. Oganessian, F.S. Abdullin, P.D. Bailey et al., Eleven new heaviest isotopes of elements $Z = 105$ to $Z = 117$ identified among the products of ^{249}Bk + ^{48}Ca reactions. Phys. Rev. C **83**, 054315 (2011). https://doi.org/10.1103/PhysRevC.83.054315
8. Y.T. Oganessian, F.S. Abdullin, S.N. Dmitriev et al., Investigation of the ^{243}Am + ^{48}Ca reaction products previously observed in the experiments on elements 113, 115, and 117. Phys. Rev. C **87**, 014302 (2013). https://doi.org/10.1103/PhysRevC.87.014302
9. Y.T. Oganessian, V.K. Utyonkov, Super-heavy element research. Rep. Prog. Phys. **78**, 036301 (2015). https://doi.org/10.1088/0034-4885/78/3/036301
10. V.K. Utyonkov, N.T. Brewer, Y.T. Oganessian et al., Experiments on the synthesis of superheavy nuclei ^{284}Fl and ^{285}Fl in the ^{239,240}Pu + ^{48}Ca reactions. Phys. Rev. C **92**, 034609 (2015). https://doi.org/10.1103/PhysRevC.92.034609
11. E.M. Holmbeck, T.M. Sprouse, M.R. Mumpower, Nucleosynthesis and observation of the heaviest elements. Eur. Phys. J. A **59**, 28 (2023). https://doi.org/10.1140/epja/s10050-023-00927-7
12. B. Lommel, C.E. Düllmann, B. Kindler et al., Status and developments of target production for research on heavy and superheavy nuclei and elements. Eur. Phys. J. A. **59**, 14 (2017). https://doi.org/10.1140/epja/s10050-023-00919-7
13. G.M. Ter-Akopian, A.S. Iljinov, Y.T. Oganessian et al., Synthesis of the new neutron-deficient isotopes ^{250}102, ^{242}Fm, and ^{254}Ku. Nucl. Phys. A **255**, 509 (1975). https://doi.org/10.1016/0375-9474(75)90696-X
14. G. Munzenberg, S. Hofmann, W. Faust et al., The new isotopes ^{247}Md, ^{243}Fm, ^{239}Cf, and investigation of the evaporation residues from fusion of ^{206}Pb, ^{208}Pb, and^{209}Bi with ^{40}Ar. Z. Phys. A **302**, 7 (1981). https://doi.org/10.1007/BF01425097
15. V. Ninov, F.P. Heßberger, S. Hofmann et al., Identification of new mendelevium and einsteinium isotopes in bombardments of ^{209}Bi with ^{40}Ar. Z. Phys. A **356**, 11 (1996). https://doi.org/10.1007/s002180050141
16. J. Khuyagbaatar, S. Hofmann, F.P. Heßberger et al., Spontaneous fission of neutron-deficient fermium isotopes and the new nucleus ^{241}Fm. Eur. Phys. J. A **37**, 177 (2008). https://doi.org/10.1140/epja/i2008-10608-4
17. O.N. Malyshev, A.V. Belozerov, M.L. Chelnokov et al., The new isotope ^{217}U. Eur. Phys. J. A **8**, 295 (2000). https://doi.org/10.1007/s100500070082
18. L. Ma, Z.Y. Zhang, Z.G. Gan et al., α-decay properties of the new isotope ^{216}U. Phys. Rev. C **91**, 051302 (2015). https://doi.org/10.1103/PhysRevC.91.051302
19. H.B. Yang, Z.Y. Zhang, J.G. Wang et al., Alpha decay of the new isotope ^{215}U. Eur. Phys. J. A **51**, 88 (2015). https://doi.org/10.1140/epja/i2015-15088-9
20. Z.Y. Zhang, Z.G. Gan, H.B. Yang et al., New isotope ^{220}Np: Probing the robustness of the $N = 126$ shell closure in neptunium. Phys. Rev. Lett. **122**, 192503 (2019). https://doi.org/10.1103/PhysRevLett.122.192503
21. M.D. Sun, Z. Liu, T.H. Huang et al., New short-lived isotope ^{223}Np and the absence of the $Z = 92$ subshell closure near $N = 126$. Phys. Lett. B **771**, 303 (2017). https://doi.org/10.1016/j.physletb.2017.03.074
22. T.H. Huang, W.Q. Zhang, M.D. Sun et al., Identi?cation of the new isotope ^{224}Np. Phys. Rev. C **98**, 044302 (2018). https://doi.org/10.1103/PhysRevC.98.044302

23. Y.T. Oganessian, V.K. Utyonkov, M.V. Shumeiko et al., Synthesis and decay properties of isotopes of element 110: ^{273}Ds and ^{275}Ds. Phys. Rev. C **109**, 054307 (2024). https://doi.org/10.1103/PhysRevC.109.054307
24. S. Bjrnholm, W.J. Swiatecki, Dynamical aspects of nucleus-nucleus collisions. Nucl. Phys. A. **391**, 471 (1982). https://doi.org/10.1016/0375-9474(82)90621-2
25. V. Zagrebaev, W. Greiner, Unified consideration of deep inelastic, quasi-fission and fusion–fission phenomena. J. Phys. G: Nucl. Part. Phys. **31**, 825 (2005). https://doi.org/10.1088/0954-3899/31/7/024
26. V. Zagrebaev, Synthesis of superheavy nuclei: Nucleon collectivization as a mechanism for compound nucleus formation. Phys. Rev. C **64**, 034606 (2001). https://doi.org/10.1103/PhysRevC.64.034606
27. K. Zhao, Z. Li, Y. Zhang et al., Production of unknown neutron-rich isotopes in ^{238}U + ^{238}U collisions at near-barrier energy. Phys. Rev. C **94**, 024601 (2016). https://doi.org/10.1103/PhysRevC.94.024601
28. G.F. Dai, L. Guo, E.G. Zhao et al., Dissipation dynamics and spin-orbit force in time-dependent Hartree-Fock theory. Phys. Rev. C **90**, 044609 (2014). https://doi.org/10.1103/PhysRevC.90.044609
29. G.G. Adamian, N.V. Antonenko, W. Scheid et al., Fusion cross sections for superheavy nuclei in the dinuclear system concept. Nucl. Phys. A **633**, 409 (1998). https://doi.org/10.1016/S0375-9474(98)00124-9
30. G.G. Adamian, N.V. Antonenkoa, W. Scheid et al., Treatment of competition between complete fusion and quasifission in collisions of heavy nuclei. Nucl. Phys. A **627**, 361 (1997). https://doi.org/10.1016/S0375-9474(97)00605-2
31. X.J. Bao, Y. Gao, J.Q. Li et al., Isotopic dependence of superheavy nuclear production in hot fusion reactions. Phys. Rev. C **92**, 034612 (2015). https://doi.org/10.1103/PhysRevC.92.034612
32. L. Zhu, J. Su, Unified description of fusion and multinucleon transfer processes within the dinuclear system model. Phys. Rev. C **104**, 044606 (2021). https://doi.org/10.1103/PhysRevC.104.044606
33. N. Antonenko, E. Cherepanov, A. Nasirov et al., Competition between complete fusion and quasi-fission in reactions between massive nuclei. The fusion barrier. Phys. Lett. B **319**, 425 (1993). https://doi.org/10.1016/0370-2693(93)91746-A
34. N.V. Antonenko, E.A. Cherepanov, A.K. Nasirov et al., Compound nucleus formation in reactions between massive nuclei: Fusion barrier. Phys. Rev. C **51**, 2635 (1995). https://doi.org/10.1103/PhysRevC.51.2635
35. A. Diaz-Torres, G.G. Adamian, N.V. Antonenko et al., Melting or nucleon transfer in fusion of heavy nuclei. Phys. Lett. B **481**, 228 (2000). https://doi.org/10.1016/S0370-2693(00)00471-8
36. M. Huang, Z. Zhang, Z. Gan et al., Dynamical deformation in heavy ion collisions and formation of superheavy nuclei. Phys. Rev. C **84**, 064619 (2011). https://doi.org/10.1103/PhysRevC.84.064619
37. X.J. Bao, S.Q. Guo, H.F. Zhang et al., Dynamics of complete and incomplete fusion in heavy ion collisions. Phys. Rev. C **97**, 024617 (2018). https://doi.org/10.1103/PhysRevC.97.024617
38. G. Giardina, S. Hofmann, A.I. Muminov et al., Effect of the entrance channel on the synthesis of superheavy elements. Eur. Phys. J. A **8**, 205–216 (2000). https://doi.org/10.1007/s10050-000-4509-7
39. P.H. Chen, H. Wu, Z.X. Yang et al., Prediction of synthesis cross sections of new moscovium isotopes in fusion?evaporation reactions. Nucl. Sci. Tech. **34**, 7 (2023). https://doi.org/10.1007/s41365-022-01157-0
40. G.J. Li, X.J. Bao, Theoretical calculations for the capture cross section of the formation of heavy and superheavy nuclei. Phys. Rev. C **107**, 024611 (2023). https://doi.org/10.1103/PhysRevC.107.024611
41. X.J. Bao, S.Q. Guo, H.F. Zhang et al., Influence of neutron excess of projectile on multinucleon transfer reactions. Phys. Lett. B **785**, 221 (2018). https://doi.org/10.1016/j.physletb.2018.08.049
42. X.J. Bao, Production of light neutron-rich nuclei in multinucleon transfer reactions. Nucl. Phys. A **986**, 60 (2019). https://doi.org/10.1016/j.nuclphysa.2019.02.009
43. S.H. Zhu, T.L. Zhao, X.J. Bao, Systematic study of the synthesis of heavy and superheavy nuclei in ^{48}Ca-induced fusion-evaporation reactions. Nucl. Sci. Tech. **35**, 124 (2024). https://doi.org/10.1007/s41365-024-01483-5
44. X.J. Bao, Possibility to produce ^{293,295,296}Og in the reactions ^{48}Ca + ^{249,250,251}Cf. Phys. Rev. C **100**, 011601(R) (2019). https://doi.org/10.1103/PhysRevC.100.011601
45. C. Riedel, G. Wolschin, W. Noerenberg, Relaxation times in dissipative heavy-ion collisions. Z. Phys. A **290**, 47 (1979). https://doi.org/10.1007/BF01408479
46. P.H. Chen, Z.Q. Feng, J.Q. Li et al., A statistical approach to describe highly excited heavy and superheavy nuclei. Chin. Phys. C **40**, 091002 (2016). https://doi.org/10.1088/1674-1137/40/9/091002
47. P.H. Chen, Production of proton-rich nuclei around $Z = 84$–90 in fusion-evaporation reactions. Eur. Phys. J. A **53**, 95 (2017). https://doi.org/10.1140/epja/i2017-12281-x
48. J.D. Jackson, A schematic model for (p, xn) cross sections in heavy elementa. Can. J. Phys. **34**, 767 (1956). https://doi.org/10.1139/p56-087
49. V. Weisskopf, Statistics and nuclear reactions. Phys. Rev. **52**, 295 (1937). https://doi.org/10.1103/PhysRev.52.295
50. A.S. Zubov, G.G. Adamian, N.V. Antonenko et al., Competition between evaporation channels in neutron-deficient nuclei. Phys. Rev. C **68**, 014616 (2003). https://doi.org/10.1103/PhysRevC.68.014616
51. N. Bohr, J.A. Wheeler, The mechanism of nuclear fission. Phys. Rev. **56**, 426 (1939). https://doi.org/10.1103/PhysRev.56.426
52. A.S. Zubov, G.G. Adamian, N.V. Antonenko et al., Survival probabilities of superheavy nuclei based on recent predictions of nuclear properties. Eur. Phys. J. A **23**, 249 (2005). https://doi.org/10.1140/epja/i2004-10089-5
53. W. Dilg, W. Schantl, H. Vonach, Level density parameters for the back-shifted fermi gas model in the mass range $40 < A < 250$. Nucl. Phys. A **217**, 269 (1973). https://doi.org/10.1016/0375-9474(73)90196-6
54. P. Moller, J.R. Nix, W.D. Myers et al., Nuclear ground-state masses and deformations. Atom. Data Nucl. Data Tabl. **59**, 185 (1995). https://doi.org/10.1006/adnd.1995.1002
55. T. Rauscher, F.K. Thielemann, K.L. Kratz, Nuclear level density and the determination of thermonuclear rates for astrophysics. Phys. Rev. C **56**, 1613 (1997). https://doi.org/10.1103/PhysRevC.56.1613
56. R.J. Charity, M.A. McMahan, G.J. Wozniak et al., Systematics of complex fragment emission in niobium-induced reactions. Nucl. Phys. A **483**, 371 (1988). https://doi.org/10.1016/0375-9474(88)90542-8
57. D. Mancusi, R.J. Charity, J. Cugnon, Unified description of fission in fusion and spallation reactions. Phys. Rev. C **82**, 044610 (2010). https://doi.org/10.1103/PhysRevC.82.044610
58. R.J. Charity, Systematic description of evaporation spectra for light and heavy compound nuclei. Phys. Rev. C **82**, 014610 (2010). https://doi.org/10.1103/PhysRevC.82.014610
59. D. Vermeulen, H.G. Clerc, C.C. Sahm et al., Cross sections for evaporation residue production near the N=126 shell closure. Z.

Physik A **318**, 157–169 (1984). https://doi.org/10.1007/BF01413464

60. D. Kamas, A. Opichal, E.V. Chernysheva et al., Evaporation-residue cross sections in complete fusion reactions leading to Hg and Rn isotopes. Phys. Rev. C **105**, 044612 (2022). https://doi.org/10.1103/PhysRevC.105.044612
61. Y. LeBeyec, R.L. Hahn, K.S. Toth et al., Reactions of ^{40}Ar with ^{160}Dy, ^{164}Dy, and ^{174}Yb. Phys. Rev. C **14**, 1038 (1976). https://doi.org/10.1103/PhysRevC.14.1038
62. X.J. Bao, Possibilities for synthesis of new neutron-deficient isotopes of superheavy nuclei. Chinese Phys. C **43**, 054105 (2019). https://doi.org/10.1088/1674-1137/43/5/054105
63. D.J. Hinde, M. Dasgupta, A new framework to investigate the systematics of fusion probabilities in heavy element formation: application to Th isotopes. Phys. Lett. B **622**, 23 (2005). https://doi.org/10.1016/j.physletb.2005.07.001
64. J. Hong, G.G. Adamian, N.V. Antonenko, Possibilities of production of transfermium nuclei in charged-particle evaporation channels. Phys. Rev. C **94**, 044606 (2016). https://doi.org/10.1103/PhysRevC.94.044606
65. Z.H. Liu, J.D. Bao, Possibility to produce element 120 in the ^{54}Cr + ^{248}Cm hot fusion reaction. Phys. Rev. C **87**, 034616 (2013). https://doi.org/10.1103/PhysRevC.87.034616
66. A.K. Nasirov, G. Mandaglio, G. Giardina et al., Effects of the entrance channel and fission barrier in synthesis of superheavy element Z=120. Phys. Rev. C **84**, 044612 (2011). https://doi.org/10.1103/PhysRevC.84.044612
67. K. Siwek-Wilczynska, T. Cap, M. Kowal et al., Predictions of the fusion-by-diffusion model for the synthesis cross sections of Z=114–120 elements based on macroscopic-microscopic fission barriers. Phys. Rev. C **86**, 014611 (2012). https://doi.org/10.1103/PhysRevC.86.014611
68. C.K. Cline, Extensions to the pre-equilibrium statistical model and a study of complex particle emission. Nucl. Phys. A **193**(2), 417 (1972). https://doi.org/10.1016/0375-9474(72)90330-2